Nanoscale

PAPER

Cite this: *Nanoscale*, 2015, **7**, 4984

In situ visualization of metallurgical reactions in nanoscale Cu/Sn diffusion couples

Qiyue Yin,[a] Fan Gao,[b] Zhiyong Gu,[b] Eric A. Stach[c] and Guangwen Zhou*[a]

Received 14th November 2014,
Accepted 6th February 2015

DOI: 10.1039/c4nr06757f

www.rsc.org/nanoscale

The Cu–Sn metallurgical soldering reaction in two-segmented Cu–Sn nanowires is studied by *in situ* transmission electron microscopy. By varying the relative lengths of Cu and Sn segments, we show that the metallurgical reaction results in a Cu–Sn solid solution for small Sn/Cu length ratio while Cu–Sn intermetallic compounds (IMCs) for larger Sn/Cu length ratios. Upon heating the nanowires to ~500 °C, two phase transformation pathways occur, η-Cu_6Sn_5 → ε-Cu_3Sn → δ-$Cu_{41}Sn_{11}$ for nanowires with a long Cu segment and η-Cu_6Sn_5 → ε-Cu_3Sn → γ-Cu_3Sn with a short Cu segment. The evolution of Kirkendall voids in the nanowires demonstrates that Cu diffuses faster than Sn in IMCs. Void growth results in the nanowire breakage that shuts off the inter-diffusion of Cu and Sn and thus leads to changes in the phase transformation pathway in the IMCs.

1. Introduction

With the development of materials synthesis and processing approaches, fabrication of well-defined nanostructures has become an everyday experience. A natural extension of this progress is to find ways to combine nanostructures of various origins, characters, and components, which requires making nanoscale contacts in these nanostructures and has become one of the main challenges in nanoscale integration.[1,2] As an essential part of electronic circuits, lead-free (Pb-free) nanosolders hold tremendous potential as a viable solution for replacing traditional tin/lead (Sn/Pb) solders which have toxic properties and may be harmful for health and the environment. Pb-free nano solders also offer exceptional opportunities for making nanoscale contacts as needed with the miniaturization of devices as well as the production of nanosized circuits. Pb-free solders have been extensively produced in bulk, powder and thin films.[3–9] Different solder nanowires such as Sn, In, Sn–Cu, Sn–Ag, have been synthesized directly using electrodeposition in nanoporous templates.[10–12] However, the knowledge of many properties of Pb-free nanosolders, including diffusion, intermetallic reaction mechanisms and phase evolution is still very limited.

Copper is the most frequently used conductor metal, and it is utilized in contact with solders because of its good solderability characteristic and excellent thermal conductivity performance. The binary copper–tin (Cu–Sn) system is one of the simplest metallurgical options for various methods of the interconnection in three-dimensional (3D) integration because of its easy formation of Cu–Sn intermetallic compounds (IMCs) that serve as the mechanical bonding between Sn-based solder and the copper pad of a printed circuit board (PCB).[13,14] The presence of a thin interfacial Cu–Sn IMC layer is essential for the bondability of the Cu pad because the IMC promotes good wetting between solder and copper.[15–20] The solder/conductor joint is weak if no metallurgical interaction occurs in the bonding, which is disastrous to electronic packaging. However, a thick IMC layer at the solder/conductor metal interface may degrade the reliability of the solder joints because the IMCs are brittle in nature and prone to generate structural defects due to the mismatches of the physical properties including elastic modulus and coefficient of thermal expansion. A thick IMC layer should be avoided during the soldering process. Thus, knowledge of the Cu–Sn interactions and phase evolution in the Cu–Sn IMCs is important to understand the reliability of solder interconnections from a metallurgical viewpoint and to optimize the soldering process.

Although the solid-state growth of Cu–Sn IMCs has been investigated extensively, almost all the previous studies have been dealt with bulk materials, which may differ significantly from the nanoscale soldering in a number of ways owing to size and geometrical effects associated with nanosolders, including the amount of solder formed at the joint, diffusion path, phase evolution of IMCs, geometry of the IMC solder joint, and formation of voids in the IMC and at the joint inter-

[a]*Department of Mechanical Engineering & Multidisciplinary Program in Materials Science and Engineering, State University of New York at Binghamton, NY 13902, USA. E-mail: gzhou@binghamton.edu*
[b]*Department of Chemical Engineering, University of Massachusetts Lowell, Lowell, MA 01854, USA*
[c]*Center for functional Nanomaterials, Brookhaven National Laboratory, Upton, NY 11973, USA*

faces. All these potential factors can significantly affect the growth and bondability of IMCs for forming stable nanoscale contacts.[21–27] By choosing two-segment Cu–Sn nanowires as a model system in which Sn acts as the solder element and Cu serves as a functional element, we aim to understand the nanoscale metallurgical soldering reaction at temperatures up to ~500 °C. Although the reflow temperature for typical soldering reactions normally does not go beyond 300 °C, it is also of fundamental interest for understanding how the IMCs such as Cu_3Sn and Cu_6Sn_5 IMCs formed at the lower temperatures evolve at high temperatures in addition to potential applications in developing solders with high temperature tolerance. Using *in situ* transmission electron microcopy (TEM) observations, we elucidate the phase/structural transformation of various IMCs and its dependence on the relative lengths of the Sn and Cu segments as well as the formation and growth of Kirkendall voids by reactive diffusion between Cu and Sn.

2. Experimental

The Cu–Sn two-segment nanowires were fabricated by room-temperature sequential electrodeposition assisted with polycarbonate nanoporous membrane templates (Whatman). Cu was deposited first using a commercial Cu plating electrolyte (Cu U-bath RTU, Technic, Inc.) with the current controlled at 2 mA cm^{-2}. After Cu plating, the Sn layer was electroplated by commercial Sn plating electrolyte (Sn concentrate with make-up solutions, Technic, Inc.) with the current controlled at 18 mA cm^{-2}. The sequential electrodeposition process was made with a continuous electrical current passing through the entire nanowire, which guaranteed the continuous growth of the Cu–Sn two-segment nanowires. After the electroplating, the polycarbonate membrane was dissolved in dichloromethane to release the nanowires into the solvent. Details of the synthesis of the nano solders can be found from previous work.[28,29] The as-prepared Cu–Sn nanowires were kept as a solution in ethanol. TEM samples were prepared by the powder sample preparation method with ultrasonic dispersion followed with drop casting onto a lacey carbon film supported by TEM Mo grid purchased from Ted Pella, which was then mounted onto a Gatan heating holder with rapid heating capability using a Gatan hot-stage temperature controller. *In situ* TEM observations of the soldering reaction in the Cu–Sn nanowires were performed using a JEOL JEM2100F transmission electron microscope operated at 200 kV. To clarify the structure of IMCs formed after the heating treatment, some of the samples were further examined by a traditional double tilt holder after rapidly cooling the samples to room temperature with a cooling rate of ~100 °C min^{-1}.

3. Results and discussion

Cu and Sn two segments are fabricated in the form of nanowires for the soldering reaction study. Fig. 1(a) shows a back-scattered scanning electron microscopy (SEM) image of the as-synthesized Cu–Sn nanowires, where the bright segments of the nanowires correspond to the Sn-rich segments while the slightly dark segments correspond to the Cu-rich segments owing to the heavier atom of Sn than Cu. Fig. 1(b) shows a scanning transmission electron microscopy (STEM) bright-field (BF) image of an as-synthesized nanowire with the corresponding energy-dispersive X-ray spectroscopy (EDS) elemental mapping shown in Fig. 1(c, d), from which the Sn and Cu segments can be easily identified. The EDS mapping reveals that the Sn segment has some intensity signal of Cu while the Cu segment has much less Sn signal, suggesting there is more interdiffusion of Cu into the Sn segment. Quantitative spot-mode EDS analyses of the compositions of the Cu and Sn segments indicate that the purity for the Cu segment is ~99% and the Sn segment has the purity of ~90%. The high purity of the two segments is also confirmed by electron diffraction analysis of the nanowire. Fig. 1(e, f) are selected area electron diffraction (SAED) patterns obtained from the Sn and Cu segments, respectively. The indexing of these patterns matches well with the crystal structures of pure Sn and Cu. These compositional and structural features of the nanowires are confirmed by checking other dozens of as-prepared Cu–Sn two segment nanowires. Both the SEM and TEM examination indicate that the as-prepared Cu–Sn nanowires are continuous without any pre-existing void or gap between the Cu and Sn segments.

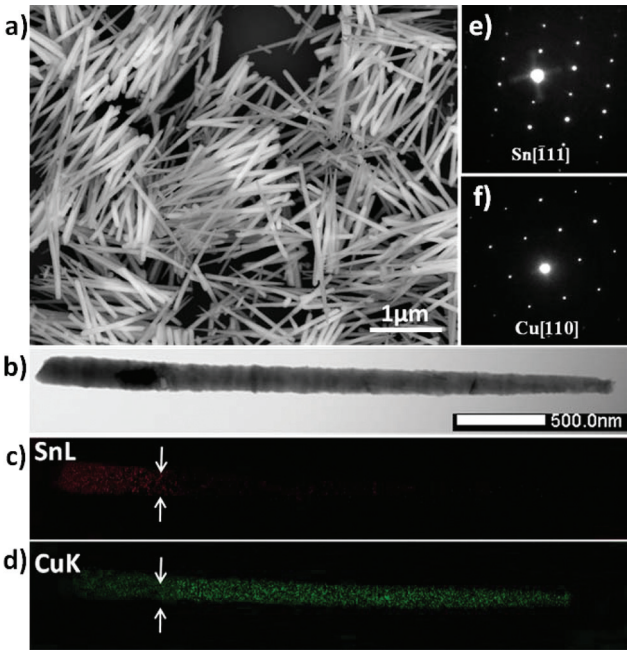

Fig. 1 As-prepared Cu–Sn two segmented nanowires by a template assisted electrodeposition method. (a) A representative SEM image of Cu–Sn two segment nanowires; (b) a STEM bright-field image of a Cu–Sn nanowire; (c, d) STEM EDS elemental mapping of the Cu–Sn nanowire shown in (b) with the Sn map in red and Cu map in blue; (e, f) selected-area electron diffraction patterns obtained from the Sn and Cu segments of the nanowire shown in (b).

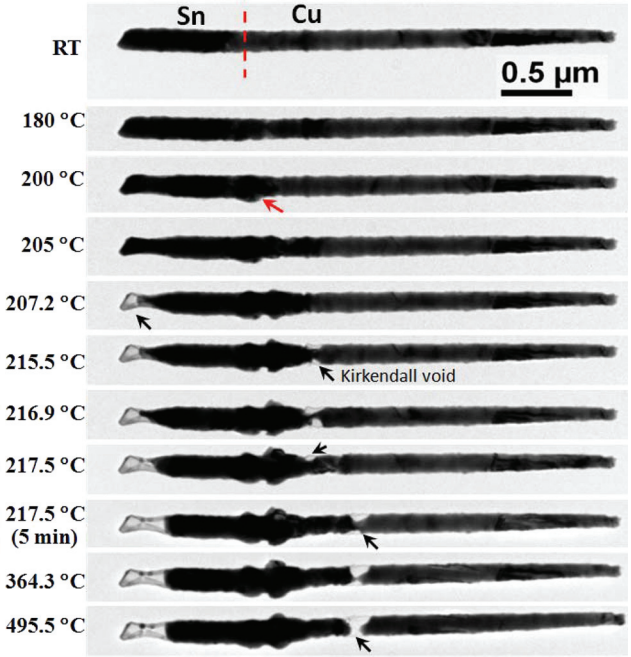

Fig. 2 *In situ* TEM observation of the morphological evolution of a Cu–Sn two segmented nanowire upon heating from room temperature (RT) to 495.5 °C. The red dashed line delineate the interface area between the Cu and Sn segment, and the Sn/Cu length ratio of the two segments is ~1 : 3. The red arrow on the TEM image corresponding to the annealing temperature of 200 °C denotes the formation of a bulge in the Cu segment near the Sn–Cu interface. The void formation in the Sn and Cu segments is denoted by black arrows at the corresponding annealing temperatures.

To study the Cu/Sn soldering reaction, a single nanowire is selected for *in situ* heating TEM observations. Fig. 2 shows the morphological evolution of a nanowire while it is being heated from room temperature (RT) to 495.5 °C with the holding time of ~1 min for each temperature interval unless specified. The dashed line denotes the original interface region of the two segments as known from the EDS analysis shown in Fig. 1(c, d, e and f), with the Sn segment on the left and the long Cu segment on the right. The Sn/Cu length ratio of the two segments is about 1 : 3. The nanowire has no obvious changes until it is being heated to ~200 °C, at which a bulge starts to become visible in the Cu segment near the Sn–Cu interface. Concurrent with the bulge formation, the diameter for the Sn segment near its end on the left is shrinking (see the corresponding TEM images at 200 °C and 205 °C). This trend becomes more obvious as the temperature is raised to 207 °C. The TEM image obtained at this temperature shows that a void is formed at the left end of the Sn segment, where the outer layer of the void is a native amorphous Sn oxide layer formed from the sample preparation. With further increase in temperature, the bulge grows larger with more Sn depleted from the end of the Sn segment, as seen from the void growth. Meanwhile, new voids are formed in the Cu segment near the bulge (see the TEM image corresponding to the temperature of 215.5 °C). The voids in the Cu segment migrate away from the bulge and merge, forming a larger void with the continued annealing at 217.5 °C for 5 min. Further increase in the annealing temperature to 364 °C and then to 495.5 °C results in the void growth that eventually leads to the breakage of the Cu segment.

The above *in situ* TEM observation reveals that the Cu–Sn metallurgical reaction occurs around 200 °C and the bulge formation around this temperature range can be attributed to the formation of the η-phase Cu_6Sn_5. The bulge formation is due to the specific volume mismatch between the resultant IMC molecule (η-Cu_6Sn_5) and the reactant elements (Cu and Sn) involved in the metallurgical reaction $6Cu + 5Sn \rightarrow Cu_6Sn_5$, where the molar volumes for Cu, Sn, and η-Cu_6Sn_5 are 7.1 cm^3 mol^{-1}, 16.29 cm^3 mol^{-1}, and 118.01 cm^3 mol^{-1}, respectively. The bulge morphology observed here also resembles the typical scallop shape of η-Cu_6Sn_5 observed in bulk solders.[21,30–36] However, as seen clearly from the *in situ* TEM images, the η-Cu_6Sn_5 bulge is formed initially in the Cu segment, suggesting that Sn diffuses into the Cu segment to form the IMC. In this case, the molar volume (V_{Cu}) of Cu is replaced with that ($V_{Cu_6Sn_5}$) of η-Cu_6Sn_5, which results in a volume expansion of 75.41 cm^3 mol^{-1} ($\Delta V = V_{Cu_6Sn_5} - 6V_{Cu}$). This large volume expansion leads to the bulge formation in the Cu segment. The observed bulge formation also suggests that the initial Cu–Sn metallurgical reaction is not dominated by Cu and Sn interdiffusion. If the η-Cu_6Sn_5 formation is dominantly controlled by Cu and Sn interdiffusion, it will lead to a volume shrinkage of −6.04 cm^3 mol^{-1} ($\Delta V = V_{Cu_6Sn_5} - 6V_{Cu} - 6V_{Sn}$). In this case, no bulge formation would be expected.

The observed bulge formation in the Cu segment is at variance with the bulk soldering reaction for which the formation of η-Cu_6Sn_5 scallops is typically attributed to the diffusion of Cu into Sn.[37–43] However, once the IMC is formed, the reaction is mainly limited to the Sn segment by Cu diffusion into Sn through the formed IMC. This is evidenced by the void formation in the Cu segment near the IMC–Cu interface due to the Kirkendall effect. Cu diffuses significantly faster than the self-diffusion of Sn[44] and Cu is also the faster diffusion component than Sn in both the Cu_3Sn and Cu_6Sn_5 phases. At 200 °C, the diffusivity of Cu in Cu_6Sn_5 is 14.2×10^{-16} m^2 s^{-1}, which is approximately 3 times greater than that of Sn in Cu_6Sn_5 (4.4×10^{-16} m^2 s^{-1}).[45,46] Similarly, the diffusivity of Cu in Cu_3Sn is approximately 2 times larger than that of Sn in Cu_3Sn (*i.e.*, 18.0×10^{-16} m^2 s^{-1} *vs.* 9.5×10^{-16} m^2 s^{-1}).[45,46] Our *in situ* TEM results of the formation of Kirkendall voids in the Cu segment and the growth behavior of IMCs are in line with the expectation based on the different diffusivities of Cu and Sn in the Cu–Sn system. With the continued IMC growth, Sn is gradually consumed by reacting with incoming Cu atoms supplied by the solid-state diffusion of Cu through the IMC layer, which results in the void growth at the end of the Sn segment. One can see that the void in the Sn segment has no noticeable change after the temperature is raised above 217.5 °C and thereafter, indicating that Sn has been completely consumed to form the IMC at this reaction stage. The continued growth of the Kirkendall void in the Cu segment at the temperature above 217.5 °C suggests that more Cu diffuses to the reacted region to

form Cu-rich IMCs while the nanowire is being heated to the higher temperatures. One can also note that the morphology and length of the Cu segment on the right of the Kirkendall void remains unchanged during the entire annealing process, demonstrating that there is little diffusion of Sn to the Cu segment due to the slower diffusion rate of Sn than Cu in the IMC.

Pure Sn has been reported to show melting-point depression when its size is below 50 nm.[47–49] The melting-point depression effect is not expected for our samples since the average diameter of the nanowires studied in our experiments is ~150 nm. Our *in situ* TEM measurements indicates that the nanowires start to melt at ~245 °C, which is ~13 °C higher than the melting point of bulk Sn. The measured higher melting point of the nanowires may be due to experimental uncertainty (±15 °C) of the temperature measurements rather than the confinement effect of the thin native oxide layer on the nanowires. The temperature measurement in our *in situ* TEM experiments is made through the use of a thermocouple that is in direct contact with the embedded heating filament of the TEM holder rather than with the sample. The measured temperature may be even a little higher than the actual specimen temperature because of heat loss during the heat transfer from the heating filament to the sample on the TEM grid. This is in line with the differential scanning calorimetry DSC measurement, which showed that pure Sn nanowires with a similar thin surface oxide layer but a smaller diameter (~50 nm) have a melting point of ~231.2 °C,[10] which is close to the melting point of bulk Sn. Therefore, both the Cu–Sn metallurgical reaction and the formation of voids in the Cu and Sn segments at the temperature below 217.5 °C shown in Fig. 2 occur in the solid state.

The nanowire shown in Fig. 2 is then rapidly cooled down to room temperature (cooling rate ~100 °C min^{-1}) from the peak temperature of 495.5 °C and the crystal structure and chemical composition of the different regions as indicated in Fig. 3(a) of the reacted Cu–Sn solder are characterized in detail by TEM. Fig. 3(b, c) are the EDS elemental maps of Cu and Sn, which show high concentration of Cu in the Sn segment while still weak intensity of Sn in the Cu segment (the zero drop of both Cu and Sn signals corresponds to the Kirkendall void formed between the two segments). The elemental mapping is consistent with the *in situ* TEM observations (Fig. 2) of the morphological evolution of the soldering reaction induced mainly by Cu diffusion through the IMC to react with Sn. Fig. 3(d, e) are SAED patterns obtained from region "1" and "2" indicated by the dashed rectangles shown in Fig. 3(a), which reveal that area "1" is ε-Cu_3Sn while area "2" is δ-$Cu_{41}Sn_{11}$. There is no particular orientation relationship between the two IMC phases. Fig. 3(f, g) show the structure models of the hexagonal superstructure (HSS) of ε-Cu_3Sn[31] and cubic δ-$Cu_{41}Sn_{11}$[50] and Fig. 3(h, i) are the simulated electron diffraction patterns of ε-Cu_3Sn[122] and δ-$Cu_{41}Sn_{11}$[311], respectively, both of which match well with the experimental diffraction patterns shown in Fig. 3(d, e). Fig. 3(j, k, l) are SAED patterns obtained from areas "3", "4", and "5" in the Cu-rich segment on the right of the Kirkendall void, as indicated in Fig. 3(a). All these patterns can be indexed well with the same zone axis [110] of Cu FCC structure with different in-plane rotations (*i.e.*, the Cu segment shows a texture structure aligned along [110] with multi twinning boundaries which are visible in the TEM BF image shown in Fig. 3(a)). Since the Cu segment contains a small amount of Sn, the structure can be regarded as α-Cu(Sn), a solid solution of Sn in Cu. In the bulk Cu–Sn phase diagram this solid solution of Sn in Cu has a composition up to 9.1 at% Sn, depending on temperature.

The Kikuchi lines and SAED pattern reveal that there are only ε-Cu_3Sn and δ-$Cu_{41}Sn_{11}$ in the reacted Sn segment, where δ-$Cu_{41}Sn_{11}$ is located adjacent to the Kirkendall void in the original Cu segment and ε-Cu_3Sn is located on the Sn end, as marked in Fig. 3(a) by the black dashed and red rectangles, respectively. The EDS line scan along the longitudinal direction of the nanowire gives three different Sn atomic compositions, 27.0%, 21.1%, 8.5%, which correspond to area 1 (ε-Cu_3Sn), area 2 (δ-$Cu_{41}Sn_{11}$), and area 3 (α-Cu), respectively. According to the Cu–Sn phase equilibrium, δ-$Cu_{41}Sn_{11}$ is a thermodynamically stable phase ranging from 350 to 590 °C,[51,52] which is formed by consuming the ε-Cu_3Sn phase formed at the lower temperature with Cu supplied from the Cu segment as the reaction temperature is raised above 217 °C, as shown in Fig. 2. The absence of the η-Cu_6Sn_5 phase in the reacted Sn segment suggests that η-Cu_6Sn_5 is completely converted to the ε-Cu_3Sn phase while only a portion of the ε-Cu_3Sn phase adjacent to the Cu segment is transformed into δ-$Cu_{41}Sn_{11}$ owing to the supply of Cu from the Cu segment at the higher temperature. To confirm that the η-Cu_6Sn_5 phase is the initial phase formed from the Cu–Sn solid state reaction, we also perform an *in situ* TEM isothermal annealing experiment of a nanowire sample at 210 °C for 20 min, as shown in Fig. 4. Fig. 4(a) is a TEM image of an un-reacted Cu–Sn nanowire at room temperature, insets are the SAED patterns confirming the presence of the Cu and Sn segments, where the Sn/Cu length ratio of the two segments is similar to that of the nanowire shown in Fig. 2., Fig. 4(b) is a TEM image of the same Cu–Sn nanowire being annealed at ~210 °C for 20 min. The Cu region (denoted by the dashed box) adjacent to the original Cu–Sn interface shows the tendency to develop into a small bulge and the electron diffraction analyses indicate that this region has the η-Cu_6Sn_5 phase while the rest of the nanowire still maintains the Sn and Cu phases One can also note that the Cu segment in the region adjacent to the η-Cu_6Sn_5 is necking and tends to develop a void. These features are consistent with those shown in Fig. 2 at the annealing temperatures around 200 °C. The structure evolution of the Cu–Sn nanowires is tracked by electron diffraction throughout the isothermal annealing process and demonstrates clearly that the Cu–Sn metallurgical reaction as well as the void development occurs in the solid state without melting the Sn segment.

Fig. 5 illustrates the *in situ* TEM observation of the morphological evolution of another Cu–Sn two segmented nanowire while it is being heated from RT to 459.8 °C. The dashed line indicates the interface area of the two segments. The Sn/Cu length ratio of the two segments is about 1 : 5, *i.e.*, the Sn

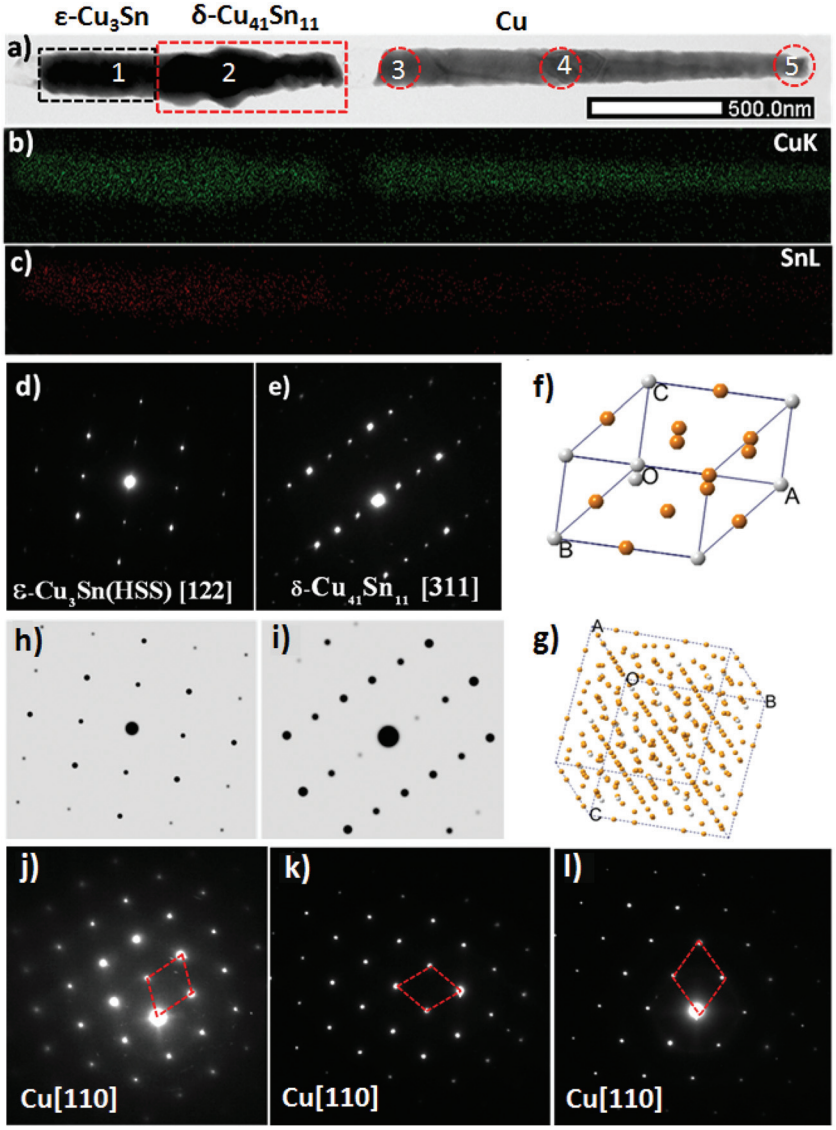

Fig. 3 Elemental mapping and structural analysis of the reacted Cu–Sn nanowire shown in Fig. 2. (a) BF-TEM image of the Cu–Sn nanowire after being annealed at 495.5 °C; (b, c) STEM EDS elemental mapping of the annealed nanowire with the Cu map in green and Sn map in red; (d, e) SAED patterns obtained from areas "1" and "2" indicated in (a), respectively; (f, g) atomic structures of ε-Cu_3Sn and δ-$Cu_{41}Sn_{11}$ used for simulating the electron diffraction patterns shown in (h and i); (j, k, l) SAED patterns obtained from areas "3", "4", and "5" indicated in (a).

segment is much shorter compared to the Cu segment. Different from the soldering reaction shown in Fig. 2, one can see that there is no any bulge formation on the nanowire annealed up to ~460 °C, suggesting that no IMC formation occurs throughout the annealing process. This is further confirmed by electron diffraction analysis of the reacted nanowire. The SAED patterns of A, B, C are obtained from the representative areas of A, B, C, respectively, as marked in the TEM image of the sample heated at 459.8 °C. The electron diffraction analyses reveal that areas A and C are α-Cu(Sn), which is a solid solution of Sn in Cu, and area B corresponds to the amorphous Sn oxide layer. While there is no IMC formation, Kirkendall voids still develop in the nanowire. As seen from the TEM image obtained at 192.6 °C, a small void (indicated by the red arrow on the TEM image) forms in the Cu segment, where a small dirt (which is the organic remnant from the sample preparation and has no effect on the soldering reaction or void formation) slightly on the right of the void serves as a marker revealing the migration of the void during the annealing process. One can see that the void first grows larger, then shrinks, and disappears at 203.5 °C, and reappears at another location of the nanowire (see the TEM image of the sample at 203.5 °C (and holding for 5 min), where a small void forms on the right side of the small dirt). The void grows larger with increasing annealing temperature, and meanwhile, another void forms on the right end of the Cu segment (see the TEM image obtained at 305.4 °C).

The formation of Kirkendall voids in the Cu segment demonstrates that the diffusion of Cu in Sn is faster than that of Sn in Cu. This is similar as the diffusion of Cu and Sn in

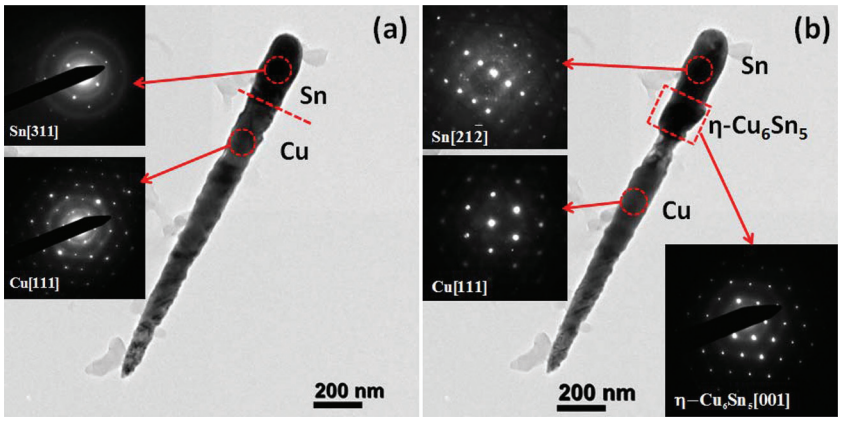

Fig. 4 Formation of η-Cu_6Sn_5 from the isothermal annealing of a Cu–Sn nanowire at ~210 °C. (a) TEM image of an unreacted Cu–Sn two-segment nanowire at room temperature, where the dashed line denotes the location of the interface between the Sn and Cu segments, insets are SAED patterns from the Cu and Sn segments; (b) TEM image of the nanowire reacted at ~210 °C for 20 min, where the η-Cu_6Sn_5 phase is formed in the original Cu segment, insets are SAED patterns obtained from the indicated regions.

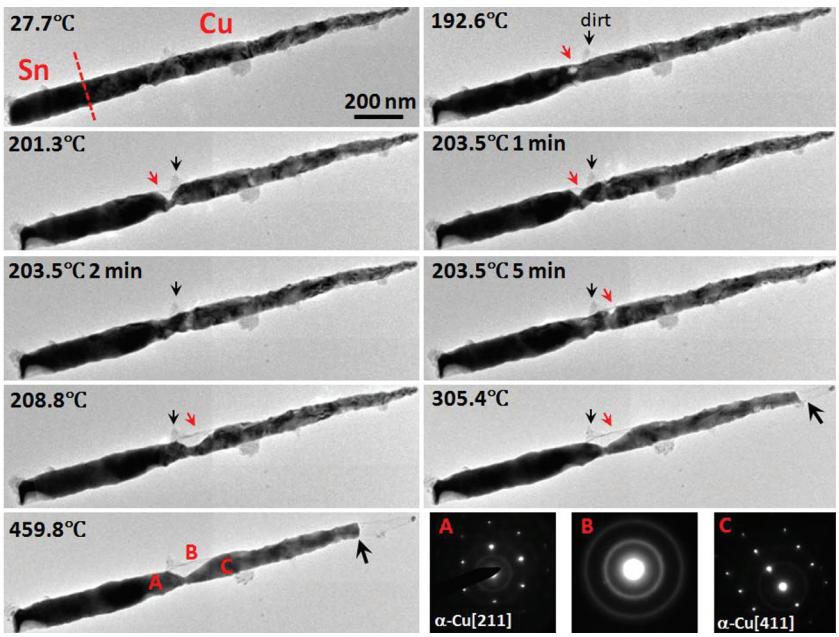

Fig. 5 *In situ* TEM observation of the morphological evolution of a Cu–Sn two segmented nanowire upon heating from RT to 495.5 °C. The red dashed line delineates the interface area between the Cu and Sn segment, and the Sn/Cu length ratio of the two segments is ~1 : 5. The red arrow denotes the formation and migration of a void in the Cu segment. The black arrow denotes the formation of another void near the end of the Cu segment. SAED patterns A, B, and C are obtained from regions A, B, and C indicated in the TEM image corresponding to the annealing temperature of 459.8 °C.

the IMC, in which Cu diffuses faster than Sn, as revealed from the *in situ* TEM observation shown in Fig. 2. Fig. 5 also reveals that the IMC formation requires the availability of sufficient amount of Sn, which depends on the relative lengths of the Cu and Sn segments. In the case shown in Fig. 5, the Sn segment is too short compared to the Cu segment, which does not allow for IMC formation. Alternatively, the fast composition homogenization of the nanowire by interdiffusion of Cu and Sn results in the formation of the solid solution of Sn in Cu.

Fig. 6 illustrates the metallurgical soldering reaction of a Cu–Sn nanowire with roughly equal length (Cu/Sn length ratio = 1 : 1) of the Cu and Sn segments. Fig. 6(a) is an STEM DF image of the nanowire before it is heated, where the Sn segment appears brighter than the Cu segment because Sn atom is heavier than Cu. Fig. 6(b) is an *in situ* STEM DF image of the nanowire heated at 491 °C, which shows that the nanowire has relatively uniform contrast, suggesting that the interdiffusion of Cu and Sn occurs along the nanowire. Fig. 6(b) also reveals the formation of several bulges on the Cu segment (this is similar as the nanowire shown in Fig. 2, where the IMC bulge forms also on the Cu segment). Fig. 6(c) is an *in situ* STEM BF image of the nanowire that is being heated at 491 °C,

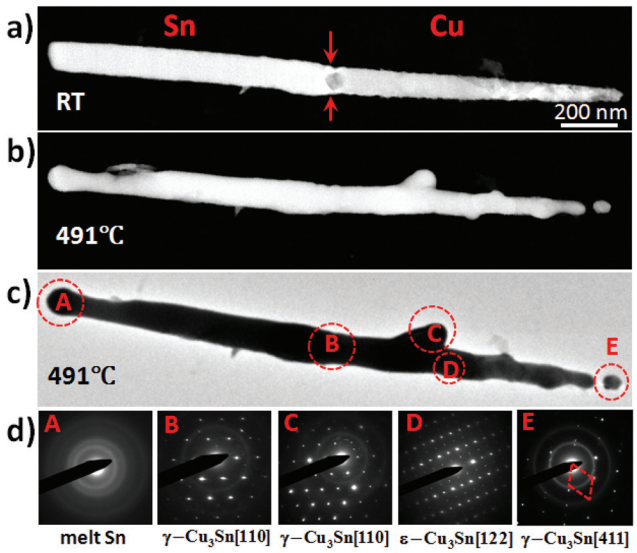

Fig. 6 Soldering reaction of a Cu–Sn nanowire with roughly equal lengths of the Cu and Sn segments (Cu/Sn length ratio ~1 : 1). (a) STEM DF image of the nanowire before annealing; (b) STEM DF image of the Cu–Sn nanowire at 491 °C; (c) TEM bright-field image of the Cu–Sn nanowire at 491 °C; (d) SAED patterns obtained from the corresponding areas indicated in (c) while the nanowire is being annealed at 491 °C.

which shows that there is a Kirkendall void on the right near the end of the Cu segment. Fig. 6(d) shows SAED patterns obtained from the representative areas of the nanowire marked in Fig. 6(c). Diffraction pattern A obtained from the area on the left end of the Sn segment shows a limited number of diffusing rings, which are typical features of an amorphous structure, demonstrating that the left end of the Sn segment is not reacted and still in its melt state at the high temperature. SAED patterns B, C, and E can be indexed well with γ-Cu_3Sn while diffraction pattern D obtained from area D matches well with ε-Cu_3Sn. The electron diffraction analysis reveals that a compound consisting of various IMC phases has been developed in the Cu segment, in which the ε-Cu_3Sn phase transforms into the high-temperature phase of γ-Cu_3Sn as the nanowire is heated up to 491 °C. The kirkendall void near the right side of the nanowire is formed during the ε-Cu_3Sn → γ-Cu_3Sn transformation at the relatively high temperature because the right end (*i.e.*, area E) has already changed to γ-Cu_3Sn (rather than un-reacted Cu). The *in situ* TEM observation also demonstrates clearly the complete reaction of the Cu segment owing to the availability of sufficient Sn (there is still remaining Sn in its melt state). The absence of the initially formed η-Cu_6Sn_5 phase suggests that it has completely transformed to Cu_3Sn by reacting with additional Cu at the elevated temperature.

To further demonstrate the effect of the relative lengths of the Cu and Sn segments on the IMC formation, Fig. 7 shows an *in situ* TEM observation of the soldering reaction of a Cu–Sn nanowire in which the Sn segment is much longer than the Cu segment (the Sn/Cu length ratio is about 7 : 5). One can see that a Kirkendall void (marked by the red arrow in the TEM images) starts to form in the Cu segment at ~186.6 °C (where a remnant organic dirt on the left of the void can serve as a marker to reveal the void growth and migration in the course of the metallurgical reaction). With slightly increasing the annealing temperature, the void grows larger first, then shrinks and disappears at ~203.7 °C, and then re-appears on

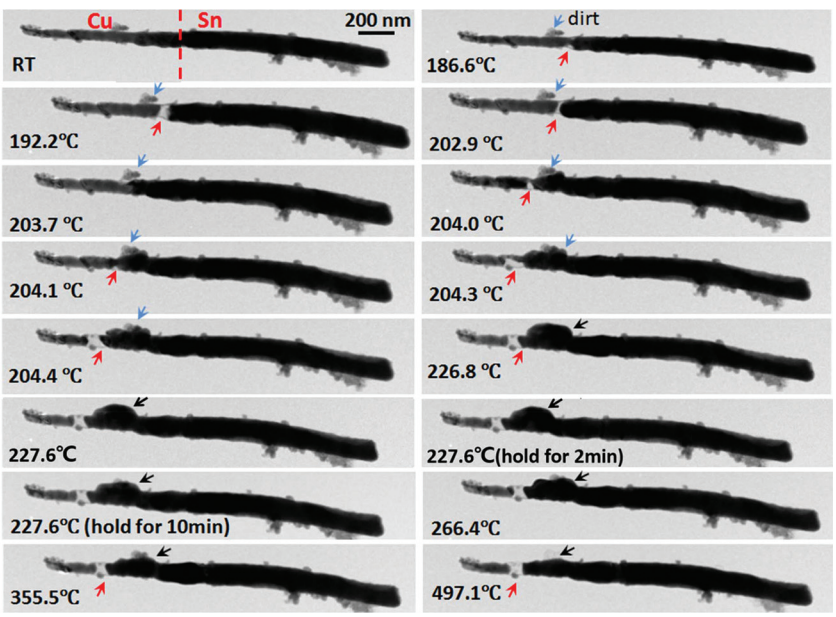

Fig. 7 *In situ* TEM observation of the morphological evolution of a Cu–Sn two segmented nanowire upon heating from RT to 497.1 °C. The red dashed line delineate the interface area between the Cu and Sn segment, and the Sn/Cu length ratio of the two segments is ~5 : 2. The red arrows denote the formation and migration of a Kirkendall void in the Cu segment, and the black arrows denote the formation, growth, and shrinkage of a bulge near the void.

the left of the dirt at 204 °C. Meanwhile, a bulge becomes clearly visible in the Cu segment adjacent to the void at ~204.3 °C and grows larger with the temperature increase to 226.8 °C. At 227.6 °C (and holding for 10 min at this temperature), one can see that the bulge shrinks. This trend continues by further increasing the soldering temperature to 497.1 °C. The *in situ* TEM images also reveal that there is no obvious change in the size of the void after the complete breakage of the nanowire at 204.4 °C.

Fig. 8 depicts the EDS elemental mapping characterization of the reacted nanowire shown in Fig. 7. Fig. 8(b) shows the Cu and Sn maps of the area indicated by the dashed rectangle on the left shown in Fig. 8(a). The Cu mapping shows that areas A, C, E have much stronger Cu intensity than areas B and D while the Sn mapping reveals that area A has much weaker Sn signal than areas B, C, D, and E. Fig. 8(c) corresponds to the Cu and Sn maps of the area indicated by the dashed rectangle on the right shown in Fig. 8(a), from which one can see that the intensities for Cu and Sn are relatively uniform, suggesting the homogenization of the composition on this end.

The composition mapping is correlated with structural analysis by electron diffraction as shown in Fig. 9. Diffraction pattern A is obtained from area A of the nanowire as seen in the TEM image in the middle panel, which reveals that area A

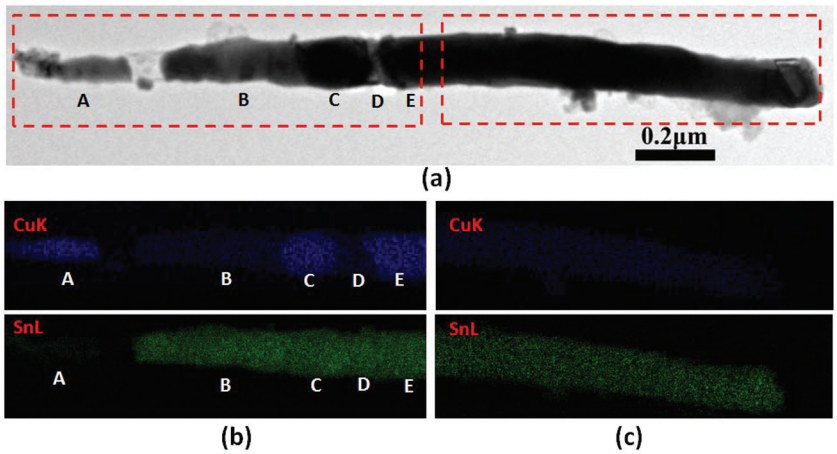

Fig. 8 Elemental mapping of the reacted Cu–Sn nanowire shown in Fig. 6. (a) A STEM BF image of the Cu–Sn nanowire after being annealed at 497.1 °C; (b) STEM EDS elemental mapping of the area indicated by the red dashed rectangle on the left shown in (a) with the Cu map in blue and Sn map in red; (c) STEM EDS elemental mapping of the area indicated by the red dashed rectangle on the right in (a).

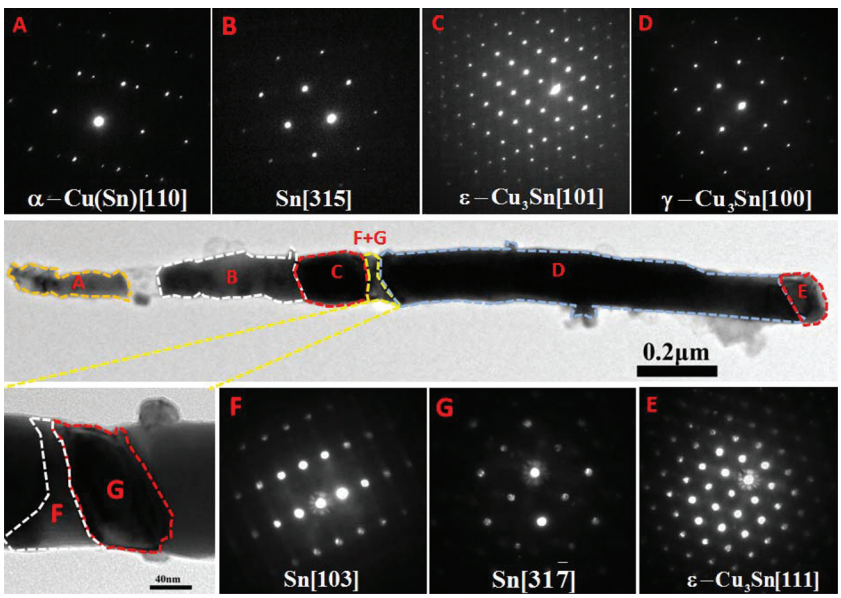

Fig. 9 Electron diffraction structural analysis of the reacted nanowire (shown in Fig. 6) after the nanowire is cooled down to room temperature. Middle panel: TEM BF image of the nanowire; upper panel: SAED patterns obtained from the corresponding areas marked on the TEM image; lower panel: on the left is a zoom-in TEM image from the indicated area, (F, G, E) are SAED patterns from the corresponding areas indicated on the TEM image.

is a solid solution of Sn in Cu. This is also consistent with the Cu and Sn mapping shown in Fig. 8(b). The formation of the Cu(Sn) solid solution suggests that the Cu segment is not completely consumed. This is because of the formation of the Kirkendall void between areas A and B, which breaks up the nanowire and thus blocks interdiffusion of Cu and Sn. Diffraction B is acquired from area B as indicated in the corresponding TEM image on the middle panel in Fig. 9, which reveals that this area is pure Sn, consistent with the Cu and Sn maps shown in Fig. 8(b). The electron diffraction patterns obtained from areas C, D and E show that areas C and E are ε-Cu_3Sn while area D is γ-Cu_3Sn. The formation of the various IMC phases is due to temperature effect, for which the η-Cu_6Sn_5 forms first and then transforms to the high-temperature phase of γ-Cu_3Sn by following the transformation path, η-Cu_6Sn_5 → ε-Cu_3Sn → γ-Cu_3Sn, with increasing the soldering temperature. The volume shrinking of the bulge starting at around 227.6 °C as seen in the *in situ* TEM images (see Fig. 7) corresponds to the η-Cu_6Sn_5 → ε-Cu_3Sn transformation. The absence of η-Cu_6Sn_5 in the reacted nanowire shown in Fig. 9 suggests that the η-Cu_6Sn_5 phase has completely transformed to ε-Cu_3Sn. Areas C and E are the remaining ε-Cu_3Sn phase. This is also consistent with the result shown in Fig. 6, which shows the co-existence of the γ-Cu_3Sn and ε-Cu_3Sn phases due to the incomplete conversion of the ε-Cu_3Sn phase. Diffraction patterns F and G are obtained from areas F and G composing of two grains as seen from the zoom-in TEM image shown on the bottom panel in Fig. 9, which indicate these areas are unreacted Sn formed in between the IMC grains.

Our *in situ* TEM observations described above reveal that the phase and morphological evolution of the Cu–Sn metallurgical reaction depends on the relative lengths of the Sn and Cu segments. A few representative length ratios of the Sn and Cu segments are examined in our *in situ* TEM experiments including the Sn/Cu length ratio of ~1 : 5 (see Fig. 5), ~1 : 3 (Fig. 2), ~1 : 1(Fig. 6), and ~7 : 5 (Fig. 7). Several trends can be drawn from the set of the samples. First, one can see that decreasing the relative length of the Sn segment leads to void formation at the end of the Sn segment due to the complete depletion of Sn for the IMC formation (Fig. 2). If the length of the Sn segment is too short, Sn forms a solid solution in Cu without IMC formation (Fig. 5). However, despite the different lengths of the two segments, Kirkendall void formation in the Cu segment always occurs due to the faster diffusion of Cu in Sn as well as in IMC than that of Sn in Cu and IMC. These voids can migrate in the Cu segment and the void growth sometimes can cause breakage of the Cu segment, which shut off the paths for the interdiffusion of Cu and Sn. Second, the bulge (η-Cu_6Sn_5) formation occurs first in the Cu segment around 200 °C, suggesting that the initial IMC formation is related to the diffusion of Sn into Cu rather than Cu diffusion into Sn. Third, increasing the length of the Sn segment results in unreacted Sn, which exists not only in the original Sn segment and but also in between IMC grains formed by interdiffusion of Cu and Sn. Fourth, increasing the annealing temperature up to ~500 °C results in two phase transformation paths, depending on the availability of Cu, *i.e.*, η-Cu_6Sn_5 → ε-Cu_3Sn → δ-$Cu_{41}Sn_{11}$ for a long Cu segment (*i.e.*, Fig. 2 and 3), and η-Cu_6Sn_5 → ε-Cu_3Sn → γ-Cu_3Sn for a shorter Cu segment (Fig. 6, 7, and 9).

Fig. 10 shows schematically the soldering reactions for the two-segment Cu–Sn nanowires with the different length ratios of the two segments. Fig. 10(a) corresponds to the reaction with a very short Sn segment, which results in the formation of a solid solution of Sn in Cu and Kirkendall voids due to the faster diffusion of Cu than Sn. Fig. 10(b) corresponds to the Cu–Sn reaction with increased length of the Sn segment, for which the Sn segment is completely consumed for IMC formation by reacting with incoming Cu. As a result, a void is formed at the end of the Sn segment. Meanwhile, a Kirkendall void is developed in the Cu segment owing to the faster diffusion of Cu than Sn in the IMCs. Fig. 10(c) illustrates the Cu–Sn reaction with similar lengths of the Cu and Sn segments, for which Cu is completely consumed to form IMCs with the concomitant formation of a Kirkendall void in the Cu segment near the end. Fig. 10(d) corresponds to the Cu–Sn reaction, where the Sn segment is longer than the Cu segment, for which both Sn and Cu are not completely consumed. The incomplete reaction of the Cu segment at the right end is due to the formation of a Kirkendall void that leads to the breakage of the Cu segment and thus shuts off the diffusion paths of Cu and Sn. The existence of un-reacted Sn is due to the lack of Cu to react with Sn. While both Fig. 10(c) and (d) represent the insufficient Cu cases, their difference in the length ratios of the Cu and Sn segments leads to different reaction products on the right end of the nanowires. In the case of equal lengths

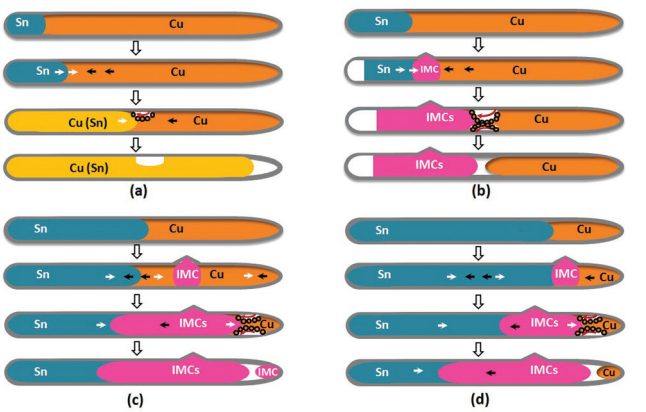

Fig. 10 Schematic showing the Cu–Sn soldering reaction of the segmented Cu–Sn nanowires with the different relative lengths of the Cu and Sn segments (the grey line represents a native oxide layer formed from the sample preparation). (a) The reaction of a long Cu segment with a small Sn segment results in the formation of a solid solution of Sn in Cu and Kirkendall voids (no IMC formation); (b) the reaction of a long Cu segment with a Sn segment with the relatively increased length results in IMC formation that consumes all the Sn segment, thereby forming a void at the end of the Sn segment; (c) reaction of the Cu–Sn nanowire with roughly equal lengths of the Cu and Sn segments results in the complete consumption of the Cu segment; (d) reaction of the Cu–Sn nanowire with a much longer Sn segment results in both incomplete Cu and Sn segments.

of the Cu and Sn segments, the nanowire breakage is induced by the ε-Cu_3Sn → γ-Cu_3Sn transformation, which leaves ε-Cu_3Sn on the right end (Fig. 10(c)). In the case of a much longer Sn segment, the nanowire breakage is induced by the Kirkendall void growth (*i.e.*, the faster diffusion of Cu to the IMCs), which shuts off the diffusion of Cu toward the IMC after the nanowire breakage and thus leaves un-reacted Cu on the right end (Fig. 10(d)), despite of the fact that the Cu segment is shorter compared to the case shown in Fig. 10(c). The IMCs formed at the peak temperature of ~500 °C shown in Fig. 10(b–d) consist of ε-Cu_3Sn, γ-Cu_3Sn, and δ-$Cu_{41}Sn_{11}$ (note that the IMC on the right end in Fig. 10(c) is a single phase of γ-Cu_3Sn due to the nanowire breakage).

Our *in situ* TEM observations of different nanowire samples with and without the presence of dirt under the same heating condition indicate that the remnant organic surface dirt has no noticeable effect on the Cu–Sn soldering reaction. However, the length ratio of the Cu and Sn segments plays an important role in determining the reaction products and morphology (*i.e.*, voiding and bulging), as summarized in Fig. 10. While we have not performed a detailed kinetic study of the IMC growth at different temperatures, the way of heating (*i.e.*, the heating rate) may likely affect the reaction pathway and morphology. For instance, prolonged isothermal annealing at different temperatures may lead to the full development of a thermodynamically favorable phase commensurate with the temperature and alloy composition, for which the reaction morphology may be different from the growth of metastable phases under a non-isothermal heating process.

The void formation proposes a big reliability threat to the mechanical strength of the joints. The formation of kirkendall voids between the Cu segment and the Sn solder joining segment is thus undesirable. Because the void formation is mainly due to the faster diffusion of Cu than that of Sn in ε-Cu_3Sn/η-Cu_6Sn_5 IMCs as well as in Sn at relative low temperatures (~200 °C), increasing temperature ramp rate and reducing the soak time of soldering reflow, or adding a barrier layer between the base metal segment and the solder segment to inhibit the diffusion of Cu into Sn may be good approaches to mitigate voiding and improve the integrity of the interconnection. During the soldering process, the IMCs formed between the solder and the base metal signify the proper bonding between solder and substrate. But excess growth of the IMC layer may result in degradation of the joint/interconnection. For the nanowire with a very short Sn segment, such as the Sn/Cu length ratio of ~1 : 5 shown in Fig. 5, there is no IMC formed, which is undesired for soldering. The nanowire with an equal or longer Sn segment results in a thicker IMC layer as compared to the one with longer Cu segment. η-Cu_6Sn_5 is the initially formed phase between the Cu and Sn segments and it may remain as the η-Cu_6Sn_5 phase or react with incoming Cu to transform into ε-Cu_3Sn, depending on the availability of Cu. η-Cu_6Sn_5 exists in two crystal structures, *i.e.*, the high-temperature hexagonal Cu_6Sn_5 and low-temperature monoclinic Cu_6Sn_5, with an allotropic transformation at ~186 °C.[53] During thermal cycling or reflow process around 250 °C, the allotropic transformation of the η-Cu_6Sn_5 hexagonal structure to the Cu_6Sn_5 monoclinic structure around 186 °C accompanies a 2.15% volume expansion,[53] which results in significant stress in the IMC layer and thus is unfavorable for the mechanical integrity of the solder joints/interconnection. This issue of the allotropic transformation induced stress in the IMC layer can be overcome by complete conversion of the hexagonal Cu_6Sn_5 phase to ε-Cu_3Sn during the soldering reaction. As shown in our TEM observation, the hexagonal η-Cu_6Sn_5 forms first between the Cu and Sn segments and then transforms to ε-Cu_3Sn given the supply of additional Cu atoms from the Cu segment. The availability of sufficient Cu atoms can facilitate the η-Cu_6Sn_5 → ε-Cu_3Sn transformation. Thus, a long Cu segment is desired for soldering because it favors the complete conversion of η-Cu_6Sn_5 to ε-Cu_3Sn during the soldering reaction.

4. Conclusions

In situ TEM has been employed to visualize the Cu–Sn soldering reaction of two-segmented Cu–Sn nanowires. We show that the formation of the Cu–Sn intermetallic compounds (IMC) and the associated phase evolution depend on the relative lengths of the Cu and Sn segments. A short Sn segment results in the formation of a solid solution of Sn in Cu. Increasing the relative length of the Sn segment leads to the formation of IMCs and Kirkendall voids in the Cu segment. Upon increasing the soldering temperature to ~500 °C, two phase transformation pathways occur, η-Cu_6Sn_5 → ε-Cu_3Sn → δ-$Cu_{41}Sn_{11}$ for a long Cu segment and η-Cu_6Sn_5 → ε-Cu_3Sn → γ-Cu_3Sn for a short Cu segment. The formation of Kirkendall voids in the Cu segments demonstrates that Cu diffuses faster than Sn in the IMCs. The breakage of the Cu segment by the void growth shuts off the inter-diffusion of Cu and Sn and thus leads to the changes in the phase transformation pathway of the IMCs.

Acknowledgements

This work was supported by the National Science Foundation under NSF Collaborative Research Award Grant CMMI-1233806. Research carried out in part at the Center for Functional Nanomaterials, Brookhaven National Laboratory, which is supported by the U.S. Department of Energy, Office of Basic Energy Sciences, under contract no. DE-AC02-98CH10886.

References

1 Y. Lin and W. Jian, *Nano Lett.*, 2008, **8**, 3146–3150.
2 Y. Peng, T. Cullis and B. Inkson, *Nano Lett.*, 2008, **9**, 91–96.
3 H. R. Kotadia, P. D. Howes and S. H. Mannan, *Microelectron. Reliab.*, 2014, **54**, 1253–1273.
4 H. Lai and J. Duh, *J. Electron. Mater.*, 2003, **32**, 215–220.

5 J. H. Pang, B. Xiong, C. Neo, X. Mang and T. Low, *Electronic Components and Technology Conference, Proceedings. 53rd*, New Orleans, LA, 2003.
6 J. Li, P. A. Agyakwa, C. M. Johnson, D. Zhang, T. Hussain and D. G. McCartney, *Surf. Coat. Technol.*, 2010, **204**, 1395–1404.
7 L. M. Lee, H. Haliman and A. A. Mohamad, *Soldering Surf. Mount Technol.*, 2013, **25**, 15–23.
8 H. Jiang, K. Moon and C. Wong, *Microelectron. Reliab.*, 2013, **53**, 1968–1978.
9 H. Jiang, K. Moon and C. Wong, *Electronic Components and Technology Conference 58th*, Lake Buena Vista, FL, 2008.
10 F. Gao, S. Mukherjee, Q. Cui and Z. Gu, *J. Phys. Chem. C*, 2009, **113**, 9546–9552.
11 Q. Cui, F. Gao, S. Mukherjee and Z. Gu, *Small*, 2009, **5**, 1246–1257.
12 J. Wang, M. Tian, T. E. Mallouk and M. H. Chan, *Nano Lett.*, 2004, **4**, 1313–1318.
13 C. K. Jin, N. B. P. Christine, C. M. Ting and D. S. Tong, *Electronics Packaging Technology Conference (EPTC) 13th*, 2011.
14 M. Alam, Y. Chan and K. Tu, *J. Appl. Phys.*, 2003, **94**, 4108–4115.
15 Y. Chan, A. C. So and J. Lai, *Mater. Sci. Eng.*, 1998, **55**, 5–13.
16 J. Yoon, C. Lee and S. Jung, *J. Electron. Mater.*, 2003, **32**, 1195–1202.
17 A. Sharif, M. Islam and Y. Chan, *Mater. Sci. Eng.*, 2004, **113**, 184–189.
18 Y. Jee, Y. Ko and J. Yu, *J. Mater. Res.*, 2007, **22**, 1879–1887.
19 C. Yu, W. Chen and J. Duh, *Intermetallics*, 2012, **26**, 11–17.
20 F. Che and J. H. Pang, *J. Alloys Compd.*, 2012, **541**, 6–13.
21 M. Islam, A. Sharif and Y. Chan, *J. Electron. Mater.*, 2005, **34**, 143–149.
22 T. Huang, H. Tseng, Y. Hsiao, C. Cheng, C. Lu and C. Liu, *Electrochem. Solid-State Lett.*, 2011, **14**, H393–H396.
23 Q. Li and Y. Chan, *J. Alloys Compd.*, 2013, **567**, 47–53.
24 W. Peng, E. Monlevade and M. E. Marques, *Microelectron. Reliab.*, 2007, **47**, 2161–2168.
25 T. Laurila, T. Mattila, V. Vuorinen, J. Karppinen, J. Li, M. Sippola and J. K. Kivilahti, *Microelectron. Reliab.*, 2007, **47**, 1135–1144.
26 T. Liu, C. Liu, Y. Huang, C. Chen and K. Tu, *Scr. Mater.*, 2013, **68**, 241–244.
27 R. Labie, W. Ruythooren and J. Van Humbeeck, *Intermetallics*, 2007, **15**, 396–403.
28 F. Gao, Z. Liu, G. Zhou, J. C. Yang and Z. Gu, *Sci. Adv. Mater.*, 2012, **4**, 881–887.
29 Q. Cui, K. Rajathurai, W. Jia, X. Li, F. Gao, Y. Lei and Z. Gu, *J. Phys. Chem. C*, 2010, **114**, 21938–21942.
30 H. Hsiao, C. Liu, H. Lin, T. Liu, C. Lu, Y. Huang, C. Chen and K. Tu, *Science*, 2012, **336**, 1007–1010.
31 J. Suh, K. Tu and N. Tamura, *J. Appl. Phys.*, 2007, **102**, 063511.
32 J. Li, P. Agyakwa and C. Johnson, *Acta Mater.*, 2011, **59**, 1198–1211.
33 D. Ma, W. Wang and S. Lahiri, *J. Appl. Phys.*, 2002, **91**, 3312–3317.
34 J. Görlich, G. Schmitz and K. N. Tu, *Appl. Phys. Lett.*, 2005, **86**, 053106.
35 X. Ma, F. Wang, Y. Qian and F. Yoshida, *Mater. Lett.*, 2003, **57**, 3361–3365.
36 J. Yoon, B. Noh, B. Kim, C. Shur and S. Jung, *J. Alloys Compd.*, 2009, **486**, 142–147.
37 B. Chao, S. Chae, X. Zhang, K. Lu, J. Im and P. Ho, *Acta Mater.*, 2007, **55**, 2805–2814.
38 A. Munding, H. Hübner, A. Kaiser, S. Penka, P. Benkart and E. Kohn, in *Wafer Level 3-D ICs Process Technology*, Springer, 2008, pp. 1–39.
39 K. Tu, *Acta Metall.*, 1973, **21**, 347–354.
40 T. Laurila, V. Vuorinen and J. Kivilahti, *Mater. Sci. Eng., R*, 2005, **49**, 1–60.
41 H. Kim and K. Tu, *Phys. Rev. B: Condens. Matter*, 1996, **53**, 16027.
42 J. Görlich, G. Schmitz and K. Tu, *Appl. Phys. Lett.*, 2005, **86**, 053106.
43 L. M. Lee and A. A. Mohamad, *Adv. Mater. Sci. Eng.*, 2013, 2013.
44 B. Dyson, T. Anthony and D. Turnbull, *J. Appl. Phys.*, 1967, **38**, 3408–3408.
45 S. Kumar, C. A. Handwerker and M. A. Dayananda, *J. Phase Equilib. Diffus.*, 2011, **32**, 309–319.
46 B. Kim, G. Lim, J. Kim, K. Lee, Y. Park and Y. Joo, *Electronic Components and Technology Conference 58th*, Lake Buena Vista, FL, 2008.
47 G. Allen, R. Bayles, W. Gile and W. Jesser, *Thin Solid Films*, 1986, **144**, 297–308.
48 S. Lai, J. Guo, V. Petrova, G. Ramanath and L. Allen, *Phys. Rev. Lett.*, 1996, **77**, 99.
49 H. Jiang, K. Moon, H. Dong, F. Hua and C. Wong, *Chem. Phys. Lett.*, 2006, **429**, 492–496.
50 P. Villars and L. D. Calvert, *Pearson's handbook of crystallographic data for intermetallic phases*, American Society for Metals Metals Park, OH, 1985.
51 N. Saunders and A. Miodownik, *Bull. Alloy Phase Diagrams*, 1990, **11**, 278–287.
52 D. Li, P. Franke, S. Fürtauer, D. Cupid and H. Flandorfer, *Intermetallics*, 2013, **34**, 148–158.
53 K. Nogita, C. Gourlay, S. McDonald, Y. Wu, J. Read and Q. Gu, *Scr. Mater.*, 2011, **65**, 922–925.